

RESEARCH ARTICLE

Macroscopic assembled graphene nanofilms based room temperature ultrafast mid-infrared photodetectors

Li Peng¹ | Lixiang Liu² | Sichao Du² | Srikrishna Chanakya Bodepudi² |
 Lingfei Li² | Wei Liu² | Runchen Lai³ | Xiaoxue Cao^{1,2} | Wenzhang Fang¹ |
 Yingjun Liu¹ | Xinyu Liu² | Jianhang Lv² | Muhammad Abid² |
 Junxue Liu³ | Shengye Jin³ | Kaifeng Wu³ | Miao-Ling Lin⁴ | Xin Cong⁴ |
 Ping-Heng Tan⁴ | Haiming Zhu⁵ | Qihua Xiong⁶ | Xiaomu Wang⁷ |
 Weida Hu⁸  | Xiangfeng Duan⁹ | Bin Yu² | Zhen Xu¹ | Yang Xu² |
 Chao Gao¹ 

¹MOE Key Laboratory of Macromolecular Synthesis and Functionalization, Department of Polymer Science and Engineering, International Research Center for X Polymers, Zhejiang University, Hangzhou, China

²School of Micro-nanoelectronics, State Key Laboratory of Silicon Materials, Hangzhou Global Scientific and Technological Innovation Center, ZJU-UIUC Joint Institute, Zhejiang University, Hangzhou, China

³State Key Laboratory of Molecular Reaction Dynamics and Dynamics, Dalian Institute of Chemical Physics, Chinese Academy of Sciences, Dalian, China

⁴State Key Laboratory of Superlattices and Microstructures, Institute of Semiconductors, Chinese Academy of Sciences, Beijing, China

⁵Department of Chemistry, Zhejiang University, Hangzhou, China

⁶Division of Physics and Applied Physics, School of Physical and Mathematical Sciences, Nanyang Technological University, Singapore, Singapore

⁷National Laboratory of Solid State Microstructures, Collaborative Innovation Center of Advanced Microstructure, School of Electronic Science and Engineering, Nanjing University, Nanjing, China

⁸State Key Laboratory of Infrared Physics, Shanghai Institute of Technical Physics, Chinese Academy of Sciences, Shanghai, China

⁹Department of Chemistry and Biochemistry, California Nanosystems Institute, University of California, Los Angeles, California, USA

Correspondence

Yang Xu, School of Micro-nanoelectronics, State Key Laboratory of Silicon Materials, Hangzhou Global Scientific and Technological Innovation Center, ZJU-UIUC Joint Institute, Zhejiang University, Hangzhou 310027, China.

Email: yangxu-isee@zju.edu.cn

Chao Gao, MOE Key Laboratory of Macromolecular Synthesis and Functionalization, Department of Polymer Science and Engineering, Zhejiang University, Hangzhou 310027, China.

Email: chaogao@zju.edu.cn

Abstract

Graphene with linear energy dispersion and weak electron–phonon interaction is highly anticipated to harvest hot electrons in a broad wavelength range. However, the limited absorption and serious backscattering of hot-electrons result in inadequate quantum yields, especially in the mid-infrared range. Here, we report a macroscopic assembled graphene (nMAG) nanofilm/silicon heterojunction for ultrafast mid-infrared photodetection. The assembled Schottky diode works in 1.5–4.0 μm at room temperature with fast response (20–30 ns, rising time, 4 mm^2 window) and high detectivity (1.6×10^{11} to 1.9×10^9 Jones from 1.5 to 4.0 μm) under the pulsed laser, outperforming single-layer-graphene/silicon photodetectors by 2–8 orders. These performances are attributed to the greatly enhanced

Li Peng and Lixiang Liu contributed equally to this work.

This is an open access article under the terms of the [Creative Commons Attribution](https://creativecommons.org/licenses/by/4.0/) License, which permits use, distribution and reproduction in any medium, provided the original work is properly cited.

© 2022 The Authors. *InfoMat* published by UESTC and John Wiley & Sons Australia, Ltd.

Funding information

National Natural Science Foundation of China, Grant/Award Numbers: 52090030, 51973191, 92164106, 61874094; China Postdoctoral Science Foundation, Grant/Award Number: 2020M681819; Fundamental Research Funds for the Central Universities, Grant/Award Numbers: K20200060, 2021FZZX001-17; Key Laboratory of Novel Adsorption and Separation Materials and Application Technology of Zhejiang Province, Grant/Award Number: 512301-I21502; Hundred Talents Program of Zhejiang University, Grant/Award Number: 188020*194231701/113

photo-thermionic effect of electrons in nMAG due to its high light absorption (~40%), long carrier relaxation time (~20 ps), low work function (4.52 eV), and suppressed carrier number fluctuation. The nMAG provides a long-range platform to understand the hot-carrier dynamics in bulk 2D materials, leading to broadband and ultrafast MIR active imaging devices at room temperature.

KEYWORDS

graphene nanofilm, heterojunction, macro-assembly, mid-infrared photodetector, photo-thermionic effect

1 | INTRODUCTION

Schottky junction, one of the most fundamental electronic junctions, plays an important role in modern optoelectronics for high-speed optical communications and photodetection^{1–4} with the merits of high-speed operation, easy integration with silicon electronics and sensors, cost-effective, and simple fabrication process. But the photoemission of energetic carriers via absorption of light by the metal layer in Schottky junctions failed in mid-infrared (MIR) light detection at room temperature. The strong electron–phonon coupling (~0.1 ps of carrier relaxation time) of metals at room temperature endows a quick dissipation of energy from hot electrons to lattices,³ resulting in lower photon energies than barrier height and ultra-low quantum yield. Some strategies like the bias-dependent barrier lowering in Schottky barrier IR diodes have extended the detection bandwidth to the mid-infrared range but these junctions suffer from low detectivity (D^*) due to the high dark current and device noise at room temperature.⁵ In addition, ill-defined barrier heights and Fermi level pinning due to metal-induced gap states further worsen the signal-to-noise ratio (SNR).^{6,7}

The single-layer graphene (SLG) with its zero-bandgap, ultrafast electron–electron interaction and weak electron–phonon coupling (~1 ps of carrier relaxation time),⁸ and dangling-bond free 2D surface, is an emerging material for room-temperature long-wavelength photodetection. The van der Waals contact of SLG with semiconductors improves the junction interface, suppressing the dark current and device noise.⁹ Nevertheless, the 2.3% light absorption and monoatomic thick scattering distance of the SLG significantly limit the hot carrier density, especially in the MIR region. Incorporating plasmonic antennas, quantum dots, and microcavity structures into the graphene/silicon (Si) system through complex

fabrication steps can improve the photon absorption and hence increase the sensitivity and/or broaden the response wavelength of the detector. Whereas, the response wavelength, response speed, and detectivity of Schottky heterojunction will be sacrificed.¹⁰

Here, we assembled graphene oxide (GO) into a wafer-scale highly-crystalline macroscopic assembled graphene nanofilm (nMAG), showing 40% light absorption and ~20 ps of carrier relaxation time. The nMAG can be integrated with Si into Schottky diodes without metal or polymer contamination. The greatly enhanced photo-thermionic (PTI) effect and lowered work function (4.52 eV) of nMAG upshift partial hot electrons from MIR to NIR region,¹¹ extending the semiconductor-determined detection limit of graphene/Si diode from 1.5 to 4.0 μm with a response speed of ~20–30 ns under the pulsed laser. Combined with the suppressed carrier number fluctuation (~3 orders lower than that of SLG) of the bulk nMAG, the nMAG/Si heterojunction shows room temperature detectivity from 1.6×10^{11} at 1.5 μm to 1.9×10^9 Jones at 4.0 μm . This work opens an avenue from commercial GO to high-performance room-temperature ultrafast mid-infrared detectors.

2 | RESULTS AND DISCUSSIONS

2.1 | Preparation strategy and structural characterization of nMAG

Figure 1A–D illustrates the preparation steps of nMAG: (I) wet-assembly of GO nanofilm and chemical reduction, (II) camphor-assisted separation, and (III) thermal annealing.¹² The obtained nMAG (4.2 cm in diameter, 45 nm thick) exhibits mobility of $\sim 1325 \text{ cm}^2 \text{ V}^{-1} \text{ s}^{-1}$ (Figure S2) due to its high crystallinity. The two-dimensional diffraction patterns in Figure 1E show all

high-order hkl reflections of nMAG, indicating a high graphitization degree of nMAG. In particular, the position of the 002 peak (2θ , 26.5°) in the corresponding 1D x-ray scattering pattern (Figure S1C) indicates an average interlayer spacing of 3.36 \AA . The graphene layers in nMAG have a perfect long-range honeycombed lattice structure without atomic-defect (Figure 1F,G), which is also verified by the undetectable O peak in the x-ray photoelectron spectroscopy curve (Figure S3) and the negligible D mode (1330 cm^{-1} , Figure 1H) in Raman spectrum. In addition, a 1.2° twisted angle between adjacent graphene layers (Figure 1G) indicates the presence of a turbostratic stacking structure. According to the 2D mode, a low fraction of decoupled structure ($I(2D_T)/(I(2D_2) + I(2D_T)) \sim 9\%$) is detected.¹³ This result is confirmed by a slightly lower wavenumber of the C mode (42.9 cm^{-1} , ~ 9 – 10 layers AB-stacked multilayer graphene stacking with twisted interface) in nMAG than that in HOPG (43.4 cm^{-1}) with a similar thickness (25 layers).¹⁴ Notably, Raman mapping within a 0.01 mm^2 (400 points, Figure S4) and spectra collected from 10 positions that evenly dispersed in a 2-in. scale exhibit a uniform

AB stacking order of 90%–93% and confirm the defect-free structure of nMAG.

2.2 | Device structure of nMAG/Si

The integration of nMAG with silicon is compatible with the back-end-of-line integration of the complementary metal-oxide-semiconductor (CMOS) technique. The free-standing nMAG was mechanically transferred onto a 2-in. silicon wafer (Figure 2A,B) by tweezers and flattened with water and nitrogen, eliminating the wrinkles and forming Schottky heterojunction with van der Waals contact.¹⁵ This contamination-free transfer process avoids metallic salt and polymer residues that are commonly observed in the SLG case.¹⁶ Nano-scale thickness endures nMAG high surface energy and thus a good adhesivity with the substrate, resulting in an atomic-scale interface contact with silicon at a $10 \text{ }\mu\text{m}$ scale (Figure 2C,D), Figures S5 and S6). Besides, the highly ordered closely-stacked structure and uniform thickness ($45 \pm 0.5 \text{ nm}$) of nMAG

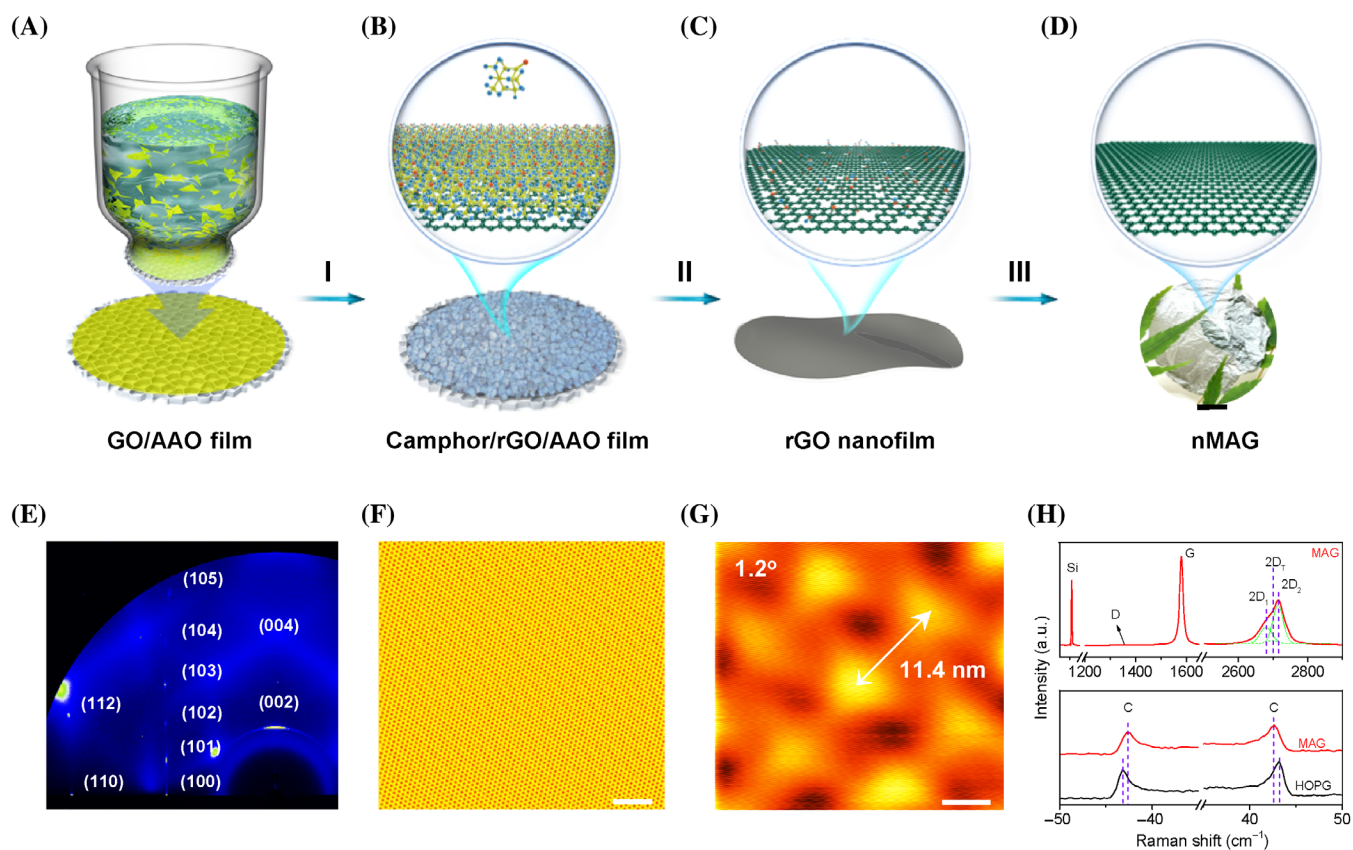


FIGURE 1 Preparation strategy and structural characterization of nMAG. (A–D) Schematic illustration of the preparation of nMAG (Text S1 and Figure S1). Blue and red balls in models represent oxygen and hydrogen elements. To enhance the contrast, the carbon element in models of camphor and GO is shown in yellow and green, respectively. (E) The grazing-incidence wide-angle x-ray scattering (GI-WAXS) patterns of nMAG (Si substrate). (F and G) Scanning-tunneling-microscopy (STM) topographic images of nMAG. (H) Raman spectra of nMAG (Si substrate). Scale bars, 1 cm D, 2 nm F, and 5 nm G

prove the efficient controllability of our assembly strategy. Furthermore, the clean transfer method avoids the interface doping and the bulk structure weakens the surface effect, endowing nMAG an intrinsic doping state (Figure S7). The nMAG has a lower work function of 4.52 ± 0.01 eV than that of SLG (4.71 eV), leading to a lower Schottky barrier height (SBH) when integrated with Si. The uniform structure and inert doping state of nMAG could reduce device-to-device variation between different pixels and batches, which satisfies the prerequisite for commercial image sensors with a large pixel density.

The thickness of nMAG ensures the enhanced light absorption that reflects in the photoresponse of nMAG/Si. The photodetection wavelength of SLG/Si diodes is limited in the visible and near-infrared range due to its limited absorption. In contrast, the nMAG/Si with enhanced light absorption shows an obvious response in the mid-infrared region. As shown in

Figures 2E and S8, the 45 nm-thick nMAG shows an extinction coefficient of 74%–81% (~40% absorption) in the wavelength range of 1–5 μm , ~20 times higher than that of SLG (1.74%–2.58%). The infrared photons absorbed by nMAG excite electron–hole pairs, which are separated and transferred from nMAG to Si under negative biases.

The nMAG-based junction exhibits a more stable normalized noise-spectral-density (NSD) $S(f)/I_{\text{dark}}^2$ than that of SLG-based junction. The high thickness and crystallinity of nMAG increase the density-of-states in the vicinity of charge-neutrality-point, strengthening the stability of the Fermi level and thus SBH of nMAG/Si. Furthermore, the thick dimension combined with the clean and atomic-scale interfacial contact with Si suppresses the carrier number fluctuation from the surface effects (traps and disorders).¹⁷ Experimental results verify that the NSD of nMAG/Si decreases with the increase in nMAG

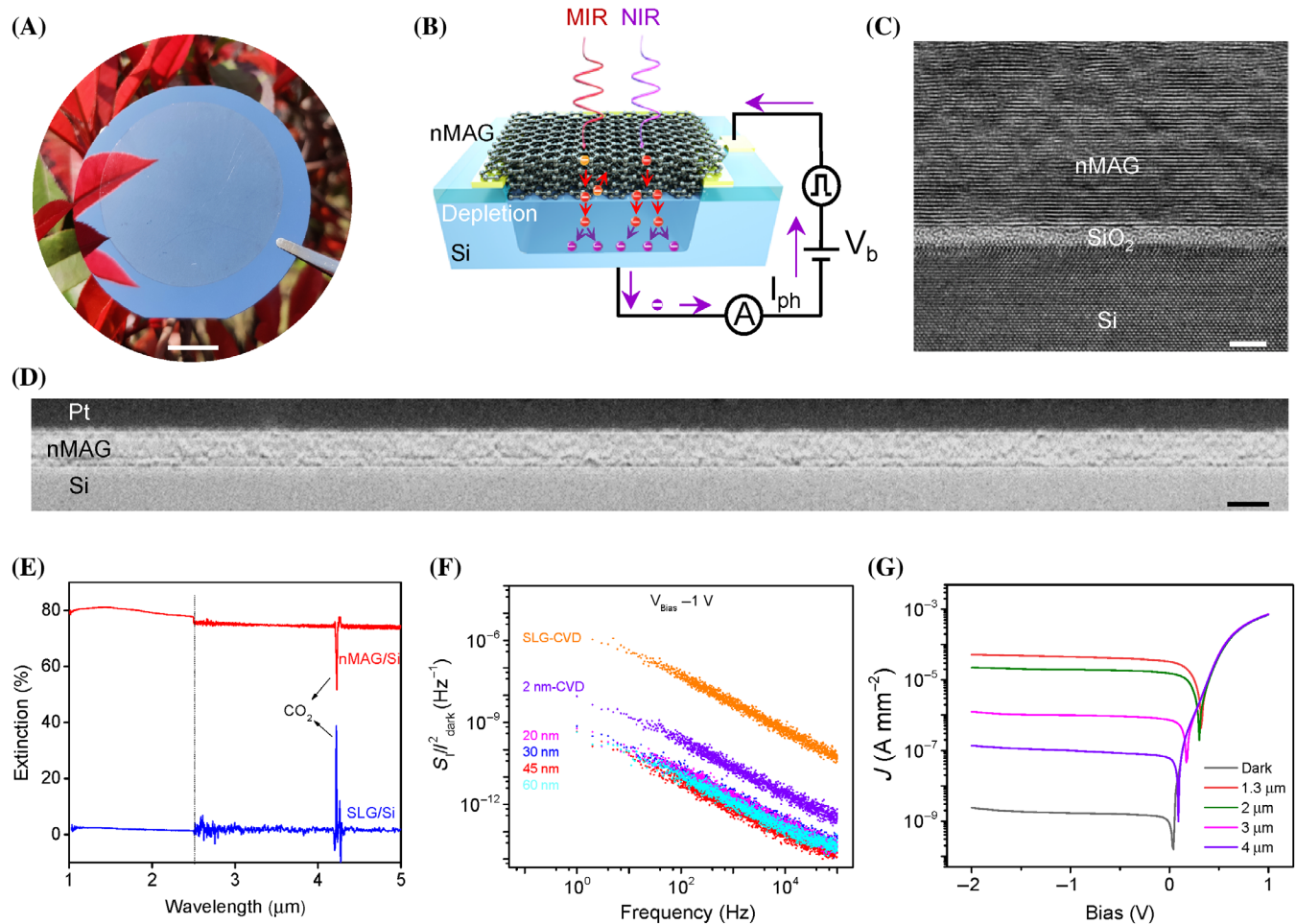


FIGURE 2 Device structural characterization of nMAG/Si. (A) The photo of the nMAG/Si wafer (2 in.). (B) A schematic of the nMAG/Si device showing the charge transport and current flow. (C) HR-TEM image of the nMAG/Si interface. (D) Cross-sectional TEM image of nMAG/Si with protected Pt layer. (E) The FTIR extinction spectra of SLG/Si and nMAG/Si. (F) Typical normalized NSD $S(f)/I_{\text{dark}}^2$ as a function of frequency at the different thicknesses of graphene films (2×2 mm² window). (G) The J - V curves of nMAG/Si under laser illumination at different wavelengths (40 mW mm^{-2} , average power density). Scale bars, 1 cm A, 2 nm C, and 50 nm D

thickness (Figure 2F). The typical NSD of 45-nm-nMAG/Si is ~ 3 orders lower than that of SLG/Si in a bias voltage from -1 to -10 V (Figure S9A,B), enabling a larger SNR for nMAG/Si.

Based on the strong light absorption, low SBH, and suppressed NSD, the nMAG/Si device features broadband photoresponse in the wavelength range of $1.5\text{--}4.0$ μm (Figure 2G). In contrast, the SLG shows a weak light absorption and a relatively short carrier relaxation time (~ 1 ps) and it is susceptible to the scattering with the substrate and interface phonons due to its large specific surface area, which limits the photo-thermionic (PTI)

emission of SLG and thus inhibits the effective harvesting of the hot carriers with energy higher than SBH,¹⁸ especially in the MIR region. Combined with the high SBH, the detectable photocurrents in SLG/Si device were observed for wavelengths ≤ 1.5 μm (Figure S9D). In brief, the lowered SBH, enhanced absorption, and suppressed noise of nMAG/Si give rise to a $\sim 2\text{--}8$ orders increase in SNR compared to SLG/Si (Figure S9C,D). The nMAG/Si device also shows a considerable photoresponse in the $5\text{--}10$ μm range (Figure S10). The negative current indicates a complicated mechanism, we will focus on this part in our future work.

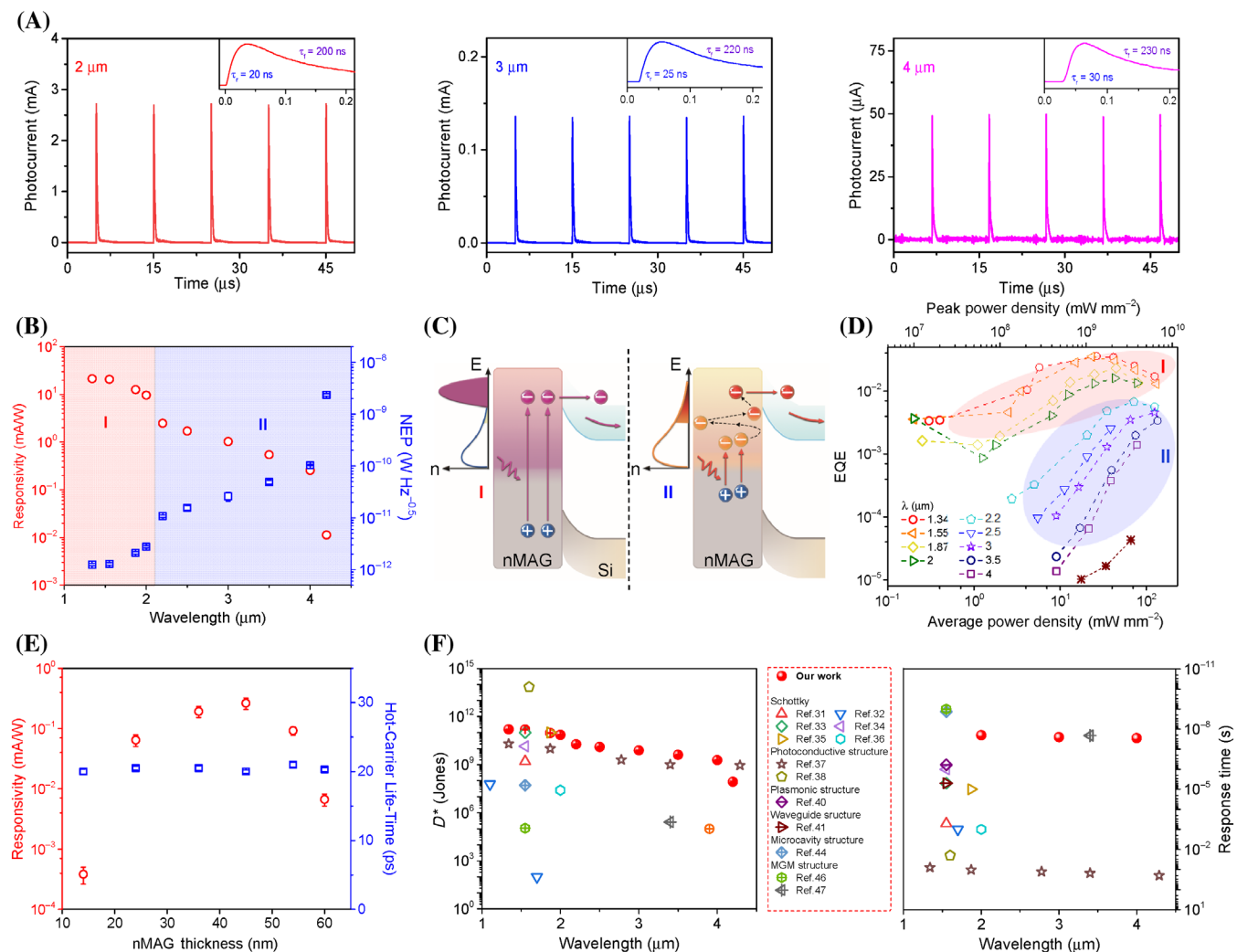


FIGURE 3 Transient photoresponse of nMAG/Si (pulsed laser, 200 fs of pulse width, 100 kHz repetition rate). (A) The photocurrent of nMAG/Si in time domain under pulsed-laser illumination at different wavelengths. (B) The responsivity and NEP of nMAG/Si as a function of laser wavelength with a fixed peak power density of 2×10^9 mW mm^{-2} (average power density, 40 mW mm^{-2} ; Note that the EQE is calculated from transient response I - t curves [peak current and peak power] and confirmed by the steady-state response I - V curves; Figure S14A,B, and Text S3). (C) The corresponding energy-band diagrams for two operation mechanisms at different wavelengths. (D) The EQE of nMAG/Si as a function of average power density at different wavelengths. (E) The responsivity and hot-carrier lifetime of nMAG/Si as a function of nMAG thickness with a fixed average power density (40 mW mm^{-2}). (F) Comparison of state-of-the-art room temperature metal and graphene-based photodetectors in terms of D^* , response time, and wavelength based on the average power density

2.3 | Transient photoresponse of nMAG/Si

As a broadband photodetector, the nMAG/Si diode displays both fast operation speed and high sensitivity. To explore the ultrafast optoelectronic dynamics in nMAG/Si, we used the femtosecond (pulse width, $\Delta t = 200$ fs) photoexcitations in MIR (Figures S11 and S12).¹⁹ We observed the response time $\tau_r \sim 20$ – 30 ns (Figure 3A) for wavelengths of 2, 3, and 4 μm , generally limited by the external circuit.²⁰ Much higher speeds can be achieved by reducing the device parasitic capacitance (Figure S13), the resistance in external circuits, or the width of the non-depleted region. Besides, the nMAG/Si exhibits a noise-equivalent-power (NEP) of 1.3×10^{-12} to 1.0×10^{-10} $\text{W Hz}^{-0.5}$ in the wavelength range of 1.3–4 μm (Figure 3B) under irradiation of pulsed laser.

The broad photoresponse beyond the intrinsic absorption of Si in nMAG/Si features two distinct working mechanisms (Figure 3C), which is confirmed by Fowler's plot (Figures 3D and S14C,D).²¹ The change on the Fowler's slope at $E \sim 0.55$ eV means that hot electrons with two signatures are generated under light irradiation with a critical wavelength of ~ 2.2 μm . The lower work function (Figure S7) endures nMAG/Si a lower SBH (~ 0.3 eV, Figure S14E,F), corresponding to a cutoff wavelength of 2.1 μm for nMAG because of its linear symmetrical band structure. For photon energies of $0.5 h\nu > \text{SBH}$ (wavelength < 2.1 μm), photoexcited electrons directly transport over the barrier and contribute to the photocurrent through the internal photoemission (IPE, regime I in Figure 3B,C),²² where the responsivity and NEP remain almost constant. When increasing the incident wavelength to 4.2 μm , the energy of photoexcited electrons is lower than SBH, so they cannot directly cross the SBH but thermalize into a Fermi–Dirac distribution. These thermalized hot-electrons with energy higher than SBH can emit into Si (PTI emission, regime II), which is confirmed by the super-linear trend of photocurrent with power ($I_{\text{ph}} \propto P^\alpha$, $\alpha > 1$) (Figure S9E).⁸ In this regime, the portion of hot-electrons with the energy higher than SBH in the Fermi–Dirac distribution drops as the incident photon energy decreases, thus lowering the responsivity and increasing NEP (Figure 3B). The photon-dominated mechanism in regime I (IPE) and regime II (PTI) enables the device to undergo a fast dynamics process. The cutoff wavelength of these two regimes can be changed and the responsivity and D^* can be optimized by tuning the doping state of the nMAG and silicon (Figure S9F) or replacing silicon with a semiconductor with higher electron affinity (χ). In addition, the PTI effect also exists in the wavelength > 4.2 μm . However, the negative effects of the enriched electron–hole pairs with lower energy than

SBH, such as electron–phonon scattering (Figure S15), screening, and so forth,^{23,24} dominate in the 5–10 μm region (Figure S10), resulting in a negative photocurrent and a thermal-dominated slow dynamics process ($\tau_r \sim 300$ ns). We will investigate this part in a separate work.

To realize the ensemble hot electron emission in graphene,^{25,26} where the electron population heats up to much higher temperatures than the lattice temperature (300 K), power densities above 0.1 MW cm^{-2} are required. For power densities lower than this value, the graphene–semiconductor junction is dominated by the single-hot electron emission ($< 0.1 \text{ MW cm}^{-2}$)²⁷ and cold-field emission ($< 1 \text{ W cm}^{-2}$), respectively. As the number of graphene layers increases, the total light absorption of nMAG increases. Whereas, the recombination of hot electrons also increases due to the scattering with the phonons while transporting from the top to the bottom layer, which significantly suppresses the population of hot electrons with higher energies than SBH.

According to Figure 3E, the significantly enhanced multiplication of hot carriers in nMAG under pulsed laser with high power densities determines the MIR detection in 1.5–4 μm . The reasons are twofold. First, the multilayer structure of nMAG provides a larger light absorption path, thus generating more photoexcited hot electrons than that of SLG. Second, nMAG can accommodate the photo-induced tunneling⁸ that distribute photoexcited carriers into multiple graphene layers before thermalization, providing a larger cross-section for carrier multiplication and hence generating more hot electrons. At the moderate electric field ($\sim 10^3 \text{ V cm}^{-1}$), a major fraction of hot-electrons in nMAG transport towards the nMAG/Si interface facilitated by, (1) long out-of-plane hot-carrier diffusion length due to the prolonged hot-carrier lifetime,²⁸ (2) non-conservation of both in-plane and out-of-plane momentum from carrier scattering in nMAG,²⁹ and (3) the momentum uncertainly due to the presence of a few misorientations in the stacking order, resulting in a finite out-of-plane velocity (v_z) for charge carriers (Figure 1F). The synergistic effect of (2–3) presumably delocalizes the electronic wave function of the carriers in nMAG beyond the Schottky barrier into silicon until the carriers experience a well-defined momentum. In the metal/Si Schottky diodes, the increased metal thickness and interface quality significantly diminish the quantum yield due to the trap states at the interface and the decrease in light absorption depth, thus longer diffusion lengths are needed for the carriers to reach the interface.⁷ In the SLG/Si case, based on the simplified Vickers-Mooney model, only a portion of hot-electrons with energy and momentum falling

within the escape cone is transferred into silicon, and the rest scatter back to SLG.³⁰ In comparison, in the nMAG/Si case, some of the backscattered hot-electrons are expected to be redirected into the escape cone through phonon and interface wall scattering due to the large available cross-section of nMAG (regime II). Therefore, the trade-off between out-of-plane charge transfer and recombination in nMAG achieves the maximum responsivity at 45 nm (Figure 3E).

In terms of speed, D^* , and broadband wavelength, the comprehensive performance of the nMAG/Si heterojunction is better than the previously reported metal and graphene-based infrared photodetectors (Figure 3F and Table S2).^{31–49} Especially, the high D^* from 1.6×10^{11} to 1.9×10^9 Jones in the 1.3–4 μm region (pulsed laser), the external circuit determined the fast response speed (~ 20 – 30 ns), room temperature operation, large area, scalability, and compatibility with Si-based CMOS technology lay the foundation of the nMAG/Si device for the practical application in near future. Our device shows an external quantum efficiency (EQE, Figure S14C) of 3.6%–1.6% in regime I and 0.5%–0.04% in regime II under the bias of -1 V. The EQE in regime II, especially under low power density, can be improved by the synergistic combination of the avalanche effect in Si and the high bias V_b (described below).

2.4 | Hot-carrier transport in nMAG/Si

To further investigate the hot-carrier dynamics in nMAG/Si, we conducted a pump-probe transient absorption measurement (Figure S16) on our detectors. The pump laser wavelength is 3.5 μm , and the probe is above the SBH from 1.2 μm to 1.6 μm . When pump laser fluence is >1 mW mm^{-2} , the scattered electron occupation close to the charge neutrality point (0.37–0.42 eV, Figure 4A) and the upshift of a fraction of hot-electrons to the energies comparable to SBH ($E > h\nu_{\text{pump}}$) are clear indications of AR.¹¹ (Note that the second peak at ~ 10 ps is due to photoexcitation from the reflected pump laser on the 500 μm -thick silicon substrate underneath.) In this fluence regime, the combination of impact excitation dominated in the initial tens of femtoseconds and AR prevailed subsequently, resulting in a large pool of hot-electrons with energies near SBH ($E \sim \phi_B$) (Figure 4A). The AR process dominates carrier kinetics in nMAG until it reaches the optical phonon bottleneck (~ 200 meV) at ~ 1 ps, and then the relaxation occurs via an interaction with acoustic phonons within ~ 20 ps as displayed in Figures 4B and S17. Due to the high crystallinity of nMAG and the non-polar property of silicon, the cooling from disorder and substrate-based surface plasmon polariton is

weak in our devices.⁵⁰ The dominant carrier relaxation mechanism gradually shifts from AR to acoustic phonon emission at longer wavelengths, confirmed by the elimination of the fast component (within 1.5 ps) in the bi-exponential fitting results (Figure 4B). If the hot electron energies are lower than the optical phonon energy (0.2 eV), the dominating relaxation process is through the emission of acoustic phonons. This requires the emission of multiple acoustic phonons for cooling energies in the range of 0.1 eV and therefore much longer relaxation times are expected. In fact, cooling via acoustic phonons releases energy in the order of less than $K_B T$ and therefore the total cooling time can even reach 100's of ps.⁵¹ Therefore, ~ 20 ps relaxation time is reasonable in nMAG with the ability to generate rich hot electrons with lower energies than optical phonon.

In real systems, hot electron scattering at disorder accelerates this cooling process in the order of $K_B T$, known as super collision cooling. To further verify this, we performed pump-probe studies on graphene with different thicknesses (Figures S17 and S18). For CVD-grown SLG, the monolayer thickness enhances the hot electrons scattering from the interface and substrate, which decreases the cooling time greatly. Combining with the weak light absorption, the PTI effect is severely suppressed consistent with the ultra-low differential transmissivity. With the increase of thickness, the light absorption and cooling time of hot carriers increase simultaneously, improving the differential transmissivity and thus the number of hot carriers with energies higher than SBH. In the CVD-grown MLG case, due to the rich defects and grain boundaries, large density hot electrons are trapped, resulting in a low differential transmissivity. Both the long cooling time and high intensity of differential transmissivity confirm the advantage of nMAG in enhancing the PTI effect. Besides, the PTI effect has a non-monotonic dependence on power density.⁵² When the power density at 4 μm is doubled, the responsivity will increase tenfold (Figure 3D).

The out-of-plane hot-electron diffusion coefficient and cooling time are $1 \text{ cm}^2 \text{ s}^{-1}$ and 20 ps, respectively. From the saturation absorption and power-dependent analysis, the two-photon or multi-photon absorption from either nMAG or Si is ruled out in our case (Figure S19). By extracting the number of hot-electrons $n(E)$ from transient absorption ΔA and the current collected from Si, the hot-electron transfer efficiency η_e (3.5 μm) between nMAG and silicon is obtained on the order of 10^{-5} – 10^{-4} under the irradiance from 5×10^8 to 2×10^9 mW mm^{-2} (peak power density). We quantified the hot electron scattering effect by calculating the hot-carrier-multiplication. The density of hot-electrons with higher energy than chemical potential exceeds that in the conduction band after photoexcitation

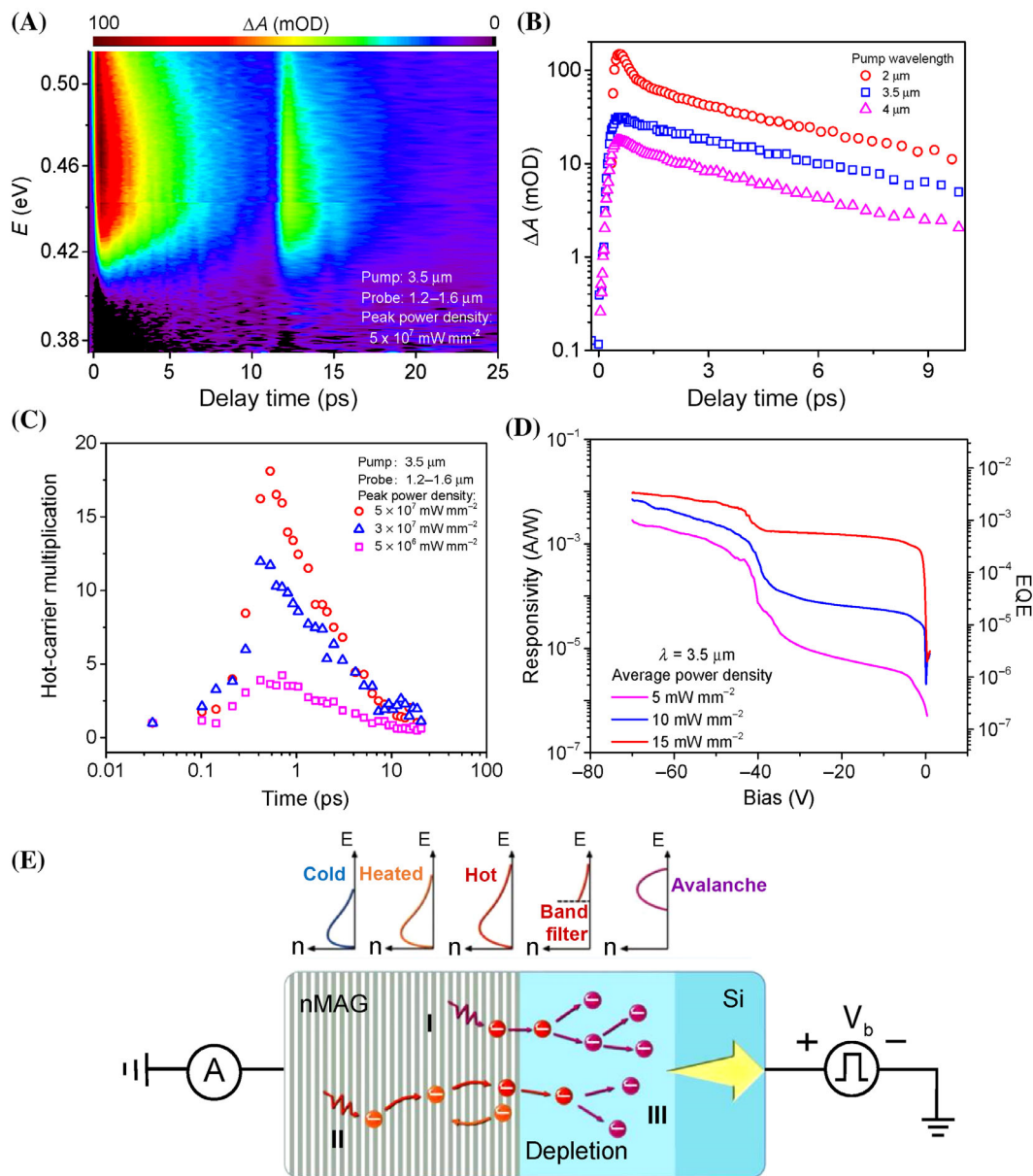


FIGURE 4 Hot-carrier transport in nMAG/Si. (A) 2D transient absorption map of nMAG/Si as functions of delay time and the half of incident photon energy. (B) The transient-absorption kinetics probed at 1.2 μm . (C) The hot-carrier multiplication factor as a function of time under different pump irradiance at 3.5 μm and probed in the range from 1.2 to 1.6 μm . (D) The responsivity and EQE of nMAG/Si as a function of bias V_b under 4 μm wavelength (Figure S19). (E) The operation mechanism schematic of nMAG/Si under 2 μm (I) and 4 μm (II) photoexcitations and avalanche (III)

with a peak multiplication value ~ 20 ($5 \times 10^7 \text{ mW mm}^{-2}$, peak power density) at 700 fs (Figure 4C). At the high electric field regime ($\sim 10^5 \text{ V cm}^{-1}$), a depleted region of $\sim 5 \mu\text{m}$ in silicon is induced, generating extra electron-hole pairs by impact ionization. The current amplification gain due to the avalanche in silicon reaches 10^2 as the bias V_b increases up to -70 V for low laser irradiance (5 mW mm^{-2} , average power density; Figure 4D,E) with an excess noise factor of 10 (Text S3). The drastic increase in current at -30 V indicates the beginning of the avalanche. As the power density increases, more photo-induced electrons are generated,

activating the avalanche at a lower voltage. This further lowers the amplification factor as the maximum current amplification no longer exclusively depends on the fixed number of ionizable electrons in the constant depletion width of Si (decided by the doping state of Si). Combining the carrier-carrier scattering in nMAG, photocurrent gain under high voltage, and carrier multiplication through the avalanche in Si, the nMAG/Si shows 1–3 orders of magnitude improvement in responsivity and EQE at 3.5 μm , reaching to 3–11 mA W^{-1} and 1–4 %, respectively. Lowering the doping concentration of the Si wafer without

changing the SBH can increase the width of the depletion region, which can further enhance the avalanche effect and thus the responsivity.

2.5 | nMAG/Si image sensors

nMAG is a promising candidate for CMOS technology due to its robust mechanical property, uniform structure, and low cost. As shown in Figure 5A, nMAG was etched into a neat array composed of $50\ \mu\text{m}$ -scale pixels by standard lithography and oxygen plasma. Combined with CMOS-compatible process flow, nMAG/Si was packed into a 9×9 -pixel array image sensor (Figures 5B and S20). According to the results of multiple photolithography, the fabrication success rate of the detectors in the array is higher than 95%. The variation of responsibility among each pixel was tested in less than one order (Figure 3B). Figure 5C presents the room temperature images captured by the nMAG/Si with a mask of the Chinese character “杭 (Hang)” at wavelengths of 1.55, 3, and $4\ \mu\text{m}$ (Figure S21). The array-level CMOS compatibility of wafer-scale nMAG offers opportunities to develop room-temperature image sensors at broad infrared wavelengths that conventional Schottky diodes are not readily applicable.

3 | CONCLUSION

This work demonstrates a high-performance nMAG/Si Schottky diode with fast response time, low NSD, and broadband response. Such outstanding detection capability is achieved by introducing high crystalline nMAG that is compatible with CMOS technology as an absorption layer, which is integrated with silicon with a clean and atomic-scale contact interface. nMAG promotes the application of the PTI effect to real devices for the first time, which greatly extends the semiconductor-determined detection wavelength of Schottky diodes. This work opens a new avenue from macroscopic defective GO to high-performance optoelectronic devices, provides a strategy to explore hot-carrier dynamics in bulk two-dimensional systems, and demonstrates a feasible way to develop low-cost and large-scale broadband graphene-based photodetectors at room temperature.

4 | MATERIALS AND METHODS

4.1 | Preparation of nMAG

nMAG was prepared from defective GO with an average size of $100\ \mu\text{m}$, provided by Hangzhou Gaoxi Technology

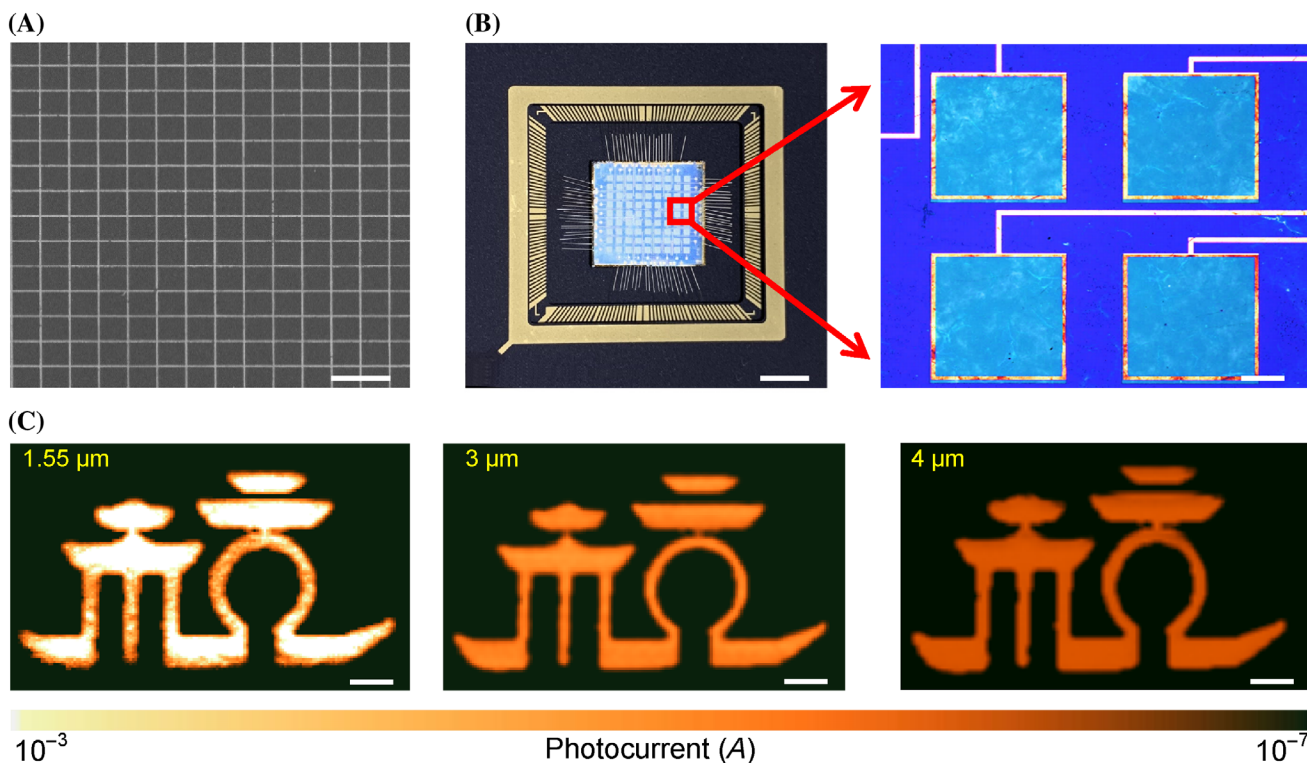


FIGURE 5 nMAG/Si image sensors. (A) SEM image of the plasma etched nMAG pixel array on silicon with a dimension of $50\ \mu\text{m} \times 50\ \mu\text{m}$ for each pixel. (B) A photo of 9×9 packed nMAG/Si image sensor with the zoomed-in optical image. (C) The scanned images of a Chinese character “杭 (Hang)” at different laser wavelengths. Scale bars, $100\ \mu\text{m}$ A, $2\ \text{mm}$ B, $200\ \mu\text{m}$ B, and $1.2\ \text{mm}$ C

Co., Ltd. (<http://www.gaoxitech.com>). The preparation method is shown in reference.¹² First, a diluted GO solution with a concentration of $4 \mu\text{g L}^{-1}$ was filtrated under vacuum by AAO filters (Whatman, pore size, $0.2 \mu\text{m}$; diameter, 48 mm) with a small contacting area below 40%. The supported GO membrane on the AAO filter was then reduced by HI vapor for 4 h in a sealed container heated under 60°C . Then the rGO/AAO membrane was placed on a bottle (diameter, 48 mm) containing camphor with the rGO side facing camphor. The bottle was then heated to 120°C to deposit camphor on the surface of the rGO film. Three to 10 min later, the camphor/rGO/AAO membrane was cooled to room temperature, and the camphor/rGO film automatically separated from the AAO membrane. The contraction effect of the camphor film during rapid cooling in the air act as the driving force, peeling the nanofilm from the substrate. Subsequently, a continuous heating process (60°C) was used to remove camphor, leaving a free-standing rGO film. Finally, the free-standing rGO film was further heated at 2800°C (heating rate of $20^\circ\text{C min}^{-1}$) for 1 h to heal defects in a high-temperature graphite furnace (NTG-SML-50L, Changsha Nuotian Electronic Technology) protected by Ar.

4.2 | Material characterizations

Raman spectra were measured in backscattering at room temperature with a Jobin-Yvon HR800 Raman system, equipped with a liquid-nitrogen-cooled CCD, a $\times 100$ objective (numerical aperture ~ 0.90), and several gratings. The excitation wavelength was 633 nm from a He-Ne laser. Plasma lines were removed from the laser using BraggGrate Bandpass filters. Measurements down to 5 cm^{-1} for the excitation were enabled by three BraggGrate notch filters with optical density 3 and $\text{FWHM} = 5\text{--}10 \text{ cm}^{-1}$. The typical laser power is $\sim 1 \text{ mW}$ to avoid sample heating. TEM images were acquired on a Hitachi H-9500 instrument operating at 300 kV . XPS was performed with a PHI 5000C ESCA System operated at 14.0 kV and all binding energies were referenced to the C 1 s neutral carbon peak at 284.6 eV . The absorption spectra were obtained by an FT-IR Spectrometer (Nicolet iN10, ThermoFisher Scientific) with a detecting diameter of $300 \mu\text{m}$. The STM experiments were performed with an ultrahigh vacuum (UHV) and a low-temperature ($\sim 77 \text{ K}$) STM system (UNISOKU USM-1500S). The samples were cleaved in the UHV chamber and immediately inserted into the measurement stage. The STM topography was conducted at a sample bias $V = -100 \text{ mV}$ and a setpoint current $I = 200 \text{ pA}$. Electron mobility was performed by Hall Effect Measurement System (Lakeshore 7604) at room

temperature with different intensities of magnetic fields applied perpendicular to the nMAG surface. The grazing incidence wide angle x-ray scattering measurements were performed at the 14b beamline of the Shanghai Synchrotron Radiation Facility in Shanghai, Republic of China. The energy of the x-rays was 18.981 keV and the wavelength was 0.653 \AA . The samples were transferred to a silicon wafer for measurement.

4.3 | Device fabrication

The device was fabricated on a lightly-doped n-type silicon wafer ($1\text{--}10 \Omega\text{-cm}$) with a 100 nm SiO_2 layer. (1) The SiO_2 layer was patterned by photolithography first. Then the e-beam deposition and thermal evaporation (Angstrom Engineering) were used to deposit Cr/Au ($5/100 \text{ nm}$) as top electrodes. (2) After lift-off, photolithography was conducted again to pattern silicon windows with a size of $2 \text{ mm} \times 2 \text{ mm}$. SiO_2 in the window was subsequently etched away with a buffered oxide etchant. The backside oxide of the silicon wafer was also etched simultaneously during this process. (3) The nMAG was transferred onto the etched silicon window by tweezers. The gap between nMAG and silicon was then filled with water to unfold the wrinkles. Finally, a flattened surface of nMAG was obtained by the purging of nitrogen before the water was completely volatilized. (4) The device was further patterned by photolithography to etch the nMAG outside the Cr/Au top electrode by oxygen plasma. (5) Finally, Ohmic contact was formed between the backside of silicon and copper tape. Au wires were then bonded with the top and back electrodes.

4.4 | Device characterization

The I - V curves were collected from Keithley Semiconductor Analyzer 2460. The device and the trans-impedance amplifier (DHPCA-100, FEMTO, 200 MHz bandwidth) were connected with an oscilloscope (Keysight DSO 9404A, 4 GHz bandwidth) to measure the photo-voltages. Periodic pulse lasers (Light Conversion, OPA-Series, $1 \mu\text{m}$ to $10 \mu\text{m}$, 200 fs pulse width, and 100 kHz repetition rate) were used as the light source. The noise spectra were recorded by a noise measurement system (PDA NC300L, 100 kHz bandwidth). Infrared bandpass filters (FB2000-500 to FB4000-500, Thorlabs) were used to filter out the stray light from the MIR laser. A calcium fluoride aspherical lens system was used to focus the infrared light on the device. The power was measured by a thermopile detector (Newport 1918-R). For the photograph, we built a scanning system

with a focused laser and a programmable X-Y stage. A data acquisition (DAQ) card was used to obtain the photocurrent data.

4.5 | Ultrafast transient absorption spectroscopy measurement

The femtosecond transient absorption setup used for this study was based on a PHAROS laser system (Light Conversion, 1030 nm, <190 fs, 200 uJ per pulse, and 100 kHz repetition rate), nonlinear frequency mixing techniques, and the Femto-TA100 spectrometer (Time-Tech Spectra). Briefly, the 1030 nm output pulse from the regenerative amplifier was split into two parts with an 80% beam splitter. The reflected part was used to pump an ORPHEUS Optical Parametric Amplifier (OPA) which generates a wavelength-tunable laser pulse from 300 to 15 μm . The transmitted 1030 nm beam was split again into two parts. One part with less than 50% was attenuated with a neutral density filter and focused into a YAG window to generate a white light continuum (WLC) from 500 to 1600 nm used for the probe beam. The probe beam was focused with an Ag parabolic reflector onto the sample. After the sample, the probe beam was collimated and then focused on a fiber-coupled spectrometer with CMOS sensors and detected at a frequency of 10 kHz. The intensity of the pump pulse used in the experiment was controlled by a variable neutral-density filter wheel. The delay between the pump and probe pulses was controlled by a motorized delay stage. The pump pulses were chopped by a synchronized chopper at 5 kHz and the absorbance change was calculated with two adjacent probe pulses (pump-blocked and pump-unblocked). All experiments were performed at room temperature.

ACKNOWLEDGMENTS

The authors would like to thank Prof. Tony Low for helpful discussions and comments. The authors also thank Dr. Zheng Li for his assistance in language modification. This work is supported by the National Natural Science Foundation of China (Nos. 52090030, 51973191, 92164106, 61874094), China Postdoctoral Science Foundation (2020M681819), Hundred Talents Program of Zhejiang University (188020*194231701/113), Key Laboratory of Novel Adsorption and Separation Materials and Application Technology of Zhejiang Province (512301-I21502), Fundamental Research Funds for the Central Universities (Nos. K20200060, 2021FZZX001-17).

CONFLICT OF INTEREST

The authors declare no conflict of interest.

ORCID

Weida Hu  <https://orcid.org/0000-0001-5278-8969>

Chao Gao  <https://orcid.org/0000-0002-3893-7224>

REFERENCES

- Bonaccorso F, Sun Z, Ferrari AC HT. Graphene photonics and optoelectronics. *Nat Photon*. 2010;4(9):611-622.
- Bartolomeo D. A graphene Schottky diodes: an experimental review of the rectifying graphene/semiconductor hetero-junction. *Phys Rep*. 2016;606:1-58.
- Sharma B. *Metal-Semiconductor Schottky Barrier Junctions and their Applications*. Boston: Springer; 1984.
- Goykhman I, Sassi U, Desiatov B, et al. On-chip integrated, silicon-graphene plasmonic Schottky photodetector with high responsivity and avalanche photogain. *Nano Lett*. 2016;16(5):3005-3013.
- Jimenez JR, Xiao X, Sturm JC, Pellegrini PW. Tunable, long-wavelength PiSi/SiGe/Si Schottky diode infrared detectors. *Appl Phys Lett*. 1995;67(4):506-508.
- Liu Y, Guo J, Zhu E, et al. Approaching the Schottky-Mott limit in van der Waals metal-semiconductor junctions. *Nature*. 2018;557(7707):696-700.
- Nishimura T, Kita K, Toriumi A. Evidence for strong Fermi-level pinning due to metal-induced gap states at metal/germanium interface. *Appl Phys Lett*. 2007;91:123123.
- Massicotte M, Schmidt P, Violla F, et al. Photo-thermionic effect in vertical graphene heterostructures. *Nat Commun*. 2016;7:12174.
- Balandin A. A low-frequency 1/f noise in graphene devices. *Nat Nanotechnol*. 2013;8(8):549-555.
- Akinwande D, Huyghebaert C, Wang C-H, et al. Graphene and two-dimensional materials for silicon technology. *Nature*. 2019;573(7775):507-518.
- Winzer T, Jago R, Malic E. Experimentally accessible signatures of Auger scattering in graphene. *Phys Rev B*. 2016;94:235430.
- Peng L, Han Y, Wang M, et al. Multifunctional macro-assembled graphene nanofilms with high crystallinity. *Adv Mater*. 2021;33:2104195.
- Cancado LG, Takai K, Enoki T, et al. Measuring the degree of stacking order in graphite by Raman spectroscopy. *Carbon*. 2008;46(2):272-275.
- Wu J-B, Zhang X, Ijaes M, et al. Resonant Raman spectroscopy of twisted multilayer graphene. *Nat Commun*. 2014;5:5309.
- Bae S-H, Kum H, Kong W, et al. Integration of bulk materials with two-dimensional materials for physical coupling and applications. *Nat Mater*. 2019;18(6):550-560.
- Gao L, Ni G-X, Liu Y, et al. Face-to-face transfer of wafer-scale graphene films. *Nature*. 2014;505(7482):190-194.
- Liu G, Rumyantsev S, Shur MS, Balandin AA. Origin of 1/f noise in graphene multilayers: surface vs. volume. *Appl Phys Lett*. 2013;102:093111.
- Chen Y, Li Y, Zhao Y, Zhu H. Highly efficient hot electron harvesting from graphene before electron-hole thermalization. *Sci Adv*. 2019;5:eaax9958.
- Massicotte M, Schmidt P, Violla F, et al. Picosecond photoresponse in van der Waals heterostructures. *Nat Nanotechnol*. 2016;11(1):42-46.
- Kniepert J, Neher D. Effect of the RC time on photocurrent transients and determination of charge carrier mobilities. *J Appl Phys*. 2017;122:195501.

21. Mooney J, Silverman J. The theory of hot-electron photoemission in Schottky-barrier IR detectors. *IEEE Trans Electron Devices*. 1985;32(1):33-39.
22. Casalino M. Internal photoemission theory: comments and theoretical limitations on the performance of near-infrared silicon Schottky photodetectors. *IEEE J Quantum Electron*. 2016;52:4000110.
23. Liu J, Xia F, Xiao D, Garcia de Abajo FJ, Sun D. Semimetals for high-performance photodetection. *Nat Mater*. 2020;19(8):830-837.
24. Tomadin A, Hornett S, Wang H, et al. The ultrafast dynamics and conductivity of photoexcited graphene at different Fermi energies. *Sci Adv*. 2018;4:eaar5313.
25. Bae JK, Bazarov I, Musumeci P, Karkare S, Padmore H, Maxson J. Brightness of femtosecond nonequilibrium photoemission in metallic photocathodes at wavelengths near the photoemission threshold. *J Appl Phys*. 2018;124:244903.
26. Maxson J, Musumeci P, Cultrera L, Karkare S, Padmore H. Ultrafast laser pulse heating of metallic photocathodes and its contribution to intrinsic emittance. *Nucl Instrum Methods Phys Res A*. 2017;865:99-104.
27. Ahsan R, Sakib MA, Chae HU, Kapadia R. Performance limits of graphene hot electron emission photoemitters. *Phys Rev Appl*. 2020;13:024060.
28. Stange A, Sohr C, Yang LX, et al. Hot electron cooling in graphite: supercollision versus hot phonon decay. *Phys Rev B*. 2015;92:184303.
29. Ang YS, Yang HY, Ang LK. Universal scaling laws in Schottky heterostructures based on two-dimensional materials. *Phys Rev Lett*. 2018;121:056802.
30. Kimata M, Denda M, Iwade S, Yutani N, Tsubouchi N. A wide spectral band photodetector with PtSi P-Si Schottky-barrier. *Int J Infrared Millimeter Waves*. 1985;6(10):1031-1041.
31. Liu X, Zhou Q, Luo S, et al. Infrared photodetector based on the photothermionic effect of graphene-nanowall/silicon heterojunction. *ACS Appl Mater Inter*. 2019;11(19):17663-17669.
32. Unsuree N, Selvi H, Crabb MG, et al. Visible and infrared photocurrent enhancement in a graphene-silicon Schottky photodetector through surface-states and electric field engineering. *2D Mater*. 2019;6:041004.
33. Cx W, Dong Y, Lu ZJ, et al. High responsivity and high-speed 1.55 μm infrared photodetector from self-powered graphene/Si heterojunction. *Sens Actuator A Phys*. 2019;291:87-92.
34. Li J, Guo Q, Zhang N, et al. Direct integration of polycrystalline graphene on silicon as a photodetector via plasma-assisted chemical vapor deposition. *J Mater Chem C*. 2018;6(36):9682-9690.
35. Du S, Ni Z, Liu X, et al. Graphene/silicon-quantum-dots/Si Schottky-pn cascade heterojunction for short-wavelength infrared photodetection. *63rd IEEE Annual International Electron Devices Meeting (IEDM)*. San Francisco, CA: IEEE Electron Devices Society; 2017.
36. Casalino M, Russo R, Russo C, et al. Free-space Schottky graphene/silicon photodetectors operating at 2 μm . *ACS Photonics*. 2018;5(11):4577-4585.
37. Du S, Lu W, Ali A, et al. A broadband fluorographene photodetector. *Adv Mater*. 2017;29:1700463.
38. Konstantatos G, Badioli M, Gaudreau L, et al. Hybrid graphene-quantum dot phototransistors with ultrahigh gain. *Nat Nanotechnol*. 2012;7(6):363-368.
39. Chen Z, Li X, Wang J, et al. Synergistic effects of plasmonics and electron trapping in graphene short-wave infrared photodetectors with ultrahigh responsivity. *ACS Nano*. 2017;11(1):430-437.
40. Ni Z, Ma L, Du S, et al. Plasmonic silicon quantum dots enabled high-sensitivity ultrabroadband photodetection of graphene-based hybrid phototransistors. *ACS Nano*. 2017;11(10):9854-9862.
41. Wang XM, Cheng ZZ, Xu K, Tsang HK, Xu JB. High-responsivity graphene/silicon-heterostructure waveguide photodetectors. *Nat Photonics*. 2013;7(11):888-891.
42. Zhu S, Yu MB, Lo GQ, Kwong DL. Near-infrared waveguide-based nickel silicide Schottky-barrier photodetector for optical communications. *Appl Phys Lett*. 2008;92:081103.
43. Casalino M, Sirlito L, Iodice M, et al. Cu/p-Si Schottky barrier-based near infrared photodetector integrated with a silicon-on-insulator waveguide. *Appl Phys Lett*. 2010;96:241112.
44. Casalino M, Sassi U, Goykhman I, et al. Vertically illuminated, resonant cavity enhanced, graphene-silicon schottky photodetectors. *ACS Nano*. 2017;11(11):10955-10963.
45. Casalino M, Coppola G, Gioffre M, et al. Cavity enhanced internal photoemission effect in silicon photodiode for sub-bandgap detection. *J Lightwave Technol*. 2010;28(22):3266-3272.
46. Mueller T, Xia F, Avouris P. Graphene photodetectors for high-speed optical communications. *Nat Photon*. 2010;4(5):297-301.
47. Yuan S, Yu R, Ma C, et al. Room temperature graphene mid-infrared bolometer with a broad operational wavelength range. *ACS Photon*. 2020;7(5):1206-1215.
48. Casalino M, Iodice M, Sirlito L, Rendina I, Coppola G. Asymmetric MSM sub-bandgap all-silicon photodetector with low dark current. *Opt Express*. 2013;21(23):28072-28082.
49. Zhu S, Chu HS, Lo GQ, Bai P, Kwong DL. Waveguide-integrated near-infrared detector with self-assembled metal silicide nanoparticles embedded in a silicon p-n junction. *Appl Phys Lett*. 2012;100:061109.
50. Graham MW, Shi SF, Ralph DC, Park J, McEuen PL. Photocurrent measurements of supercollision cooling in graphene. *Nat Phys*. 2013;9(2):103-108.
51. Song J, Reizer M, Levitov L. Disorder-assisted electron-phonon scattering and cooling pathways in graphene. *Phys Rev Lett*. 2012;109:106602.
52. Rodriguez-Nieva J, Dresselhaus M, Song J. Enhanced thermionic-dominated photoresponse in graphene Schottky junctions. *Nano Lett*. 2016;16(10):6036-6041.

SUPPORTING INFORMATION

Additional supporting information may be found in the online version of the article at the publisher's website.

How to cite this article: Peng L, Liu L, Du S, et al. Macroscopic assembled graphene nanofilms based room temperature ultrafast mid-infrared photodetectors. *InfoMat*. 2022;4(6):e12309. doi:10.1002/inf2.12309